Journal of
Applied Remote Sensing

Outer circular synthetic apeture radar imaging based on Maxwell's equations

Bing Sun
Zhijun Qiao
Jie Chen

Outer circular synthetic apeture radar imaging based on Maxwell's equations

Bing Sun,[a] Zhijun Qiao,[b] and Jie Chen[a]
[a]Beihang University, School of Electronic and Information, Beijing 100191, China
sun8839@gmail.com
[b]The University of Texas-Pan American, Department of Mathematics, Edinburg, Texas 78539-2999

Abstract. A general synthetic aperture radar (SAR) signal model based on the Maxwell's equations is derived, and three approximations are discussed for engineering applications. Based on this signal model, a novel operation of SAR, called outer circular synthetic aperture radar (Outer-CSAR), is investigated for wide observation. The Outer-CSAR works similarly to the general circular SAR, but the beam of the SAR antenna points at the outer of the circle instead of the inner. The signal model and imaging algorithm are presented for the Outer-CSAR, and furthermore, simulation is given to validate the signal model and imaging algorithm. © *2012 Society of Photo-Optical Instrumentation Engineers (SPIE).* [DOI: 10.1117/1.JRS.6.063547]

Keywords: SAR; Outer-CSAR; Maxwell's equations; signal model; approximation.

Paper 12011 received Jan. 12, 2012; revised manuscript received Apr. 10, 2012; accepted for publication May 22, 2012; published online Jun. 27, 2012.

1 Introduction

Synthetic aperture radar (SAR) has been developed in many different operations since the 1950s. The classic operations include strip-map operation, spotlight operations, ScanSAR operation,[1] TopSAR operation,[2] and so on. Under these operations the platform of SAR usually moves along a straight line while it illustrates the targets. These SAR systems are referred to as linear SAR.[3] These linear SARs are used in many fields, such as soil moisture, forestry, wetland, and agriculture by many researchers[4–16] Another operation, called circular SAR (CSAR),[3] has been presented to observe targets from many different azimuth angles. The CSAR platform moves along a circle at some altitude and stares at the targets near the nadir of the circle centered on the ground. Usually the resolution of CSAR is much higher than those of the linear operations. In this paper, we present a new operation based on the CSAR. The platform of SAR moves along a circle and the beam of the antenna points to the outer circle. That means the SAR works from the original left (or right) side-looking to the right (or left) side-looking. While the platform moves along a circle fully, a cirque scene can be illustrated. It will usually generate a bigger SAR image than the linear SARs or CSAR at the same velocity. Of course, the observing efficiency is at the expense of the decreasing resolution.

Before we discuss the signal model and image reconstruction, the general signal model will be derived from Maxwell's equations.[17,18] As we know, the received signal of SAR is generated by the microwave around the receiving antenna, and all the fields of microwave satisfy Maxwell's equations. The image formation will reconstruct the scene from the received signals. So the image reconstruction is an inverse problem of electromagnetic wave propagation.[19,20] The mathematical signal model is derived from the scattered field, and the approximations for the engineering application are presented including antenna pattern approximation, far-field approximation, and amplitude approximation for narrow band signal. According to this model, the detail of the signal model for outer-CSAR is investigated, and the image reconstruction with simulation is given.

0091-3286/2012/$25.00 © 2012 SPIE

2 General SAR Signal Model Based on Maxwell's Equations

2.1 *Maxwell's Equations*

Rather than the Maxwell's equations in vector form, the simplified scalar model is used here for our study.[21,22]

$$[\nabla^2 - c^{-2}(\mathbf{x})\partial_t^2]\varepsilon^{\text{tot}}(t,\mathbf{x}) = -j(t,\mathbf{x}), \tag{1}$$

where $\mathbf{x}$ is the three-dimensional position vector, $c(\mathbf{x})$ is the local propagation speed of eletromagnetic waves, and $c(\mathbf{x}) = c_0$ in free space (usually, c_0 is the speed of light), $\varepsilon^{\text{tot}}(t,\mathbf{x})$ and $j(t,\mathbf{x})$ are the total scalar field and the current density on the antenna, respectively. $c(\mathbf{x})$ statisfies

$$\frac{1}{c^2(\mathbf{x})} = \frac{1}{c_0^2} - V(\mathbf{x}), \tag{2}$$

where $V(\mathbf{x})$ stands for the target reflectivity function $\varepsilon^{\text{tot}}(t,\mathbf{x}) = \varepsilon^{\text{in}}(t,\mathbf{x}) + \varepsilon^{\text{sc}}(t,\mathbf{x})$, where $\varepsilon^{\text{in}}(t,\mathbf{x})$ and $\varepsilon^{\text{sc}}(t,\mathbf{x})$ are the incident scalar field and the scattered scalar field, and $\varepsilon^{\text{in}}(t,\mathbf{x})$ satisfies

$$(\nabla^2 - c_0^{-2}\partial_t^2)\varepsilon^{\text{in}}(t,\mathbf{x}) = -j(t,\mathbf{x}). \tag{3}$$

So, we can get the scattered field and the incident field as follows

$$\varepsilon^{\text{sc}}(t,\mathbf{x}) = \iint g(t-\tau,\mathbf{x}-\mathbf{z})V(\mathbf{z})\partial_\tau^2\varepsilon^{\text{tot}}(\tau,\mathbf{x})\mathrm{d}\tau\mathrm{d}\mathbf{z}, \tag{4}$$

$$\varepsilon^{\text{in}}(t,\mathbf{x}) = -\iint g(t-\tau,\mathbf{x}-\mathbf{z})j(\tau,\mathbf{x})\mathrm{d}\tau\mathrm{d}\mathbf{z}, \tag{5}$$

where $g(t,\mathbf{x}) = \frac{\delta(t-|\mathbf{x}|/c_0)}{4\pi|\mathbf{x}|}$, called Green's function, is the fundamental solution of the partial differential equation $(\nabla^2 - c_0^{-2}\partial_t^2)g(t,\mathbf{x}) = -\delta(t)\delta(\mathbf{x})$.[23]

Imposing Neumann series and Born approximation (or called the signal scattering approximation)[19,24] on Eq. (4), the scattered field is reduced to

$$\varepsilon^{\text{sc}}(t,\mathbf{x}) \approx \varepsilon_B^{\text{sc}}(t,\mathbf{x}) = \iint g(t-\tau,\mathbf{x}-\mathbf{z})V(\mathbf{z})\partial_\tau^2\varepsilon^{\text{in}}(\tau,\mathbf{x})\mathrm{d}\tau\mathrm{d}\mathbf{z}. \tag{6}$$

For simplicity, let us analyze the equations in frequency domain ω

$$E_B^{\text{sc}}(\omega,\mathbf{x}) = -\int G(\omega,\mathbf{x})V(\mathbf{z})\omega^2 E^{\text{in}}(\omega,\mathbf{x})\mathrm{d}\mathbf{z}, \tag{7}$$

where $k = \frac{\omega}{c}$, $E^{\text{in}}(\omega,\mathbf{x})$ is the Fourier transform of $\varepsilon^{\text{in}}(t,\mathbf{x})$ given by,

$$E^{\text{in}}(\omega,\mathbf{x}) = \int G(\omega,\mathbf{x}-\mathbf{y})J(\omega,\mathbf{y})\mathrm{d}\mathbf{y} \tag{8}$$

where $G(\omega,\mathbf{x}) = \frac{e^{-ik|\mathbf{x}|}}{4\pi|\mathbf{x}|}$ is the frequency expression of Green's function $g(t,\mathbf{x})$, $J(\omega,\mathbf{x})$ is the current source in frequency domain. So, we have

$$E_B^{\text{sc}}(\omega,\mathbf{x}) = -\iint G(\omega,\mathbf{x}-\mathbf{z})G(\omega,\mathbf{x}-\mathbf{y})V(\mathbf{z})\omega^2 J(\omega,\mathbf{y})\mathrm{d}\mathbf{y}\mathrm{d}\mathbf{z}. \tag{9}$$

2.2 *Mathematical Signal Model*

2.2.1 *Radiation pattern for a SAR antenna*

Suppose a planar radar antenna is set up and the current density $\boldsymbol{I}$ is constant over an aperture $[-a,a]\times[-b,b]$ in the plane formed by $\widehat{e_1}$ and $\widehat{e_2}$, then the radiation scalar $F(k,\mathbf{x})$ can be expressed by[19]

$$F(k,\mathbf{x})=\int_{-a}^{a}\int_{-b}^{b}e^{ik\hat{\mathbf{x}}\cdot(s_1\widehat{e_1}+s_2\widehat{e_2})}I\mathrm{d}s_1\mathrm{d}s_2=I[2a\,\mathrm{sinc}(ka\hat{\mathbf{x}}\cdot\widehat{e_2})][2b\,\mathrm{sinc}(kb\hat{\mathbf{x}}\cdot\widehat{e_1})], \tag{10}$$

where $\mathrm{sinc}(x)=\frac{\sin(\pi x)}{\pi x}$, $\hat{e}=(\hat{e}_1,\hat{e}_2)$ is corresponding to the antenna direction.

Let $p(t)$ be the transmitted signal, then the current density on antenna $j(t,\mathbf{x})$ is proportional to $p(t)$ and independent of position. So, $J(\omega,\mathbf{x})$ is proportional to the spectrum of transmitted signal $P(\omega)$. Then

$$F(k,\mathbf{x})=P(\omega)[2a\,\mathrm{sinc}(ka\hat{\mathbf{x}}\cdot\widehat{e_2})][2b\,\mathrm{sinc}(kb\hat{\mathbf{x}}\cdot\widehat{e_1})]=P(\omega)G_a(k,\hat{\mathbf{x}},\hat{e})\approx P(\omega)G_a(k_0,\hat{\mathbf{x}},\hat{e}), \tag{11}$$

where $k_0=\frac{\omega_0}{c}$ is the wavenumber corresponding to the carrier-frequency, and $G_a(k_0,\hat{\mathbf{x}},\hat{e})$ is just an amplitude function independent of the transmitted signal.

2.2.2 *Mathematic model of received signal*

Suppose that the antenna is located at $\mathbf{x}_0$, the incident $E^{\mathrm{in}}(\omega,\mathbf{x})$, and scattered the field $E_B^{\mathrm{sc}}(\omega,\mathbf{x})$ are

$$E^{\mathrm{in}}(\omega,\mathbf{x})=\int_{\mathbf{y}\in\mathrm{antenna}}\frac{e^{-ik|\mathbf{x}-\mathbf{y}|}}{4\pi|\mathbf{x}-\mathbf{y}|}P(\omega)\mathrm{d}\mathbf{y}\approx\frac{e^{-ik|\mathbf{x}-\mathbf{x}_0|}}{4\pi|\mathbf{x}-\mathbf{x}_0|}F(k,\mathbf{x}\widehat{-}\mathbf{x}_0), \tag{12}$$

$$E_B^{\mathrm{sc}}(\omega,\mathbf{x})\approx-\int_{\mathbf{z}\in\mathrm{target}}\frac{e^{-ik|\mathbf{x}-\mathbf{z}|}}{4\pi|\mathbf{x}-\mathbf{z}|}V(\mathbf{z})\omega^2\frac{e^{-ik|\mathbf{z}-\mathbf{x}_0|}}{4\pi|\mathbf{z}-\mathbf{x}_0|}F(k,\mathbf{x}\widehat{-}\mathbf{x}_0)\mathrm{d}\mathbf{z}. \tag{13}$$

When a monostatic SAR receives echoes, the stop-go approximation is applied and therefore the received signal is expressed by

$$S_{\mathrm{rec}}(\omega)=\int_{\mathbf{y}\in\mathrm{antenna}}E_B^{\mathrm{sc}}(\omega,\mathbf{y})\mathrm{W}(\omega,\mathbf{y})\mathrm{d}\mathbf{y}. \tag{14}$$

Using Eq. (13) in Eq. (14), we have

$$D_{\mathrm{rec}}(\omega)=-\int_{\mathbf{z}\in\mathrm{target}}\left[\int_{\mathbf{y}\in\mathrm{antenna}}\frac{e^{-ik|\mathbf{y}-\mathbf{z}|}}{4\pi|\mathbf{y}-\mathbf{z}|}W(\omega,\mathbf{y})\mathrm{d}\mathbf{y}\right]\frac{V(\mathbf{z})\omega^2e^{-ik|\mathbf{z}-\mathbf{x}_0|}}{4\pi|\mathbf{z}-\mathbf{x}_0|}F(k,\mathbf{z}\widehat{-}\mathbf{x}_0)\mathrm{d}\mathbf{z}. \tag{15}$$

In the above equation, $|\mathbf{y}-\mathbf{z}|\approx|\mathbf{z}-\mathbf{x}_0|-(\mathbf{z}\widehat{-}\mathbf{x}_0)\cdot(\mathbf{y}-\mathbf{x}_0)$ and $\frac{1}{|\mathbf{y}-\mathbf{z}|}\approx\frac{1}{|\mathbf{z}-\mathbf{x}_0|}$ are adopted to produce the following form

$$D_{\mathrm{rec}}(\omega)\approx-\int_{\mathbf{z}\in\mathrm{target}}\left[\int_{\mathbf{y}\in\mathrm{antenna}}e^{ik(\mathbf{z}\widehat{-}\mathbf{x}_0)\cdot(\mathbf{y}-\mathbf{x}_0)}W(\omega,\mathbf{y})\mathrm{d}\mathbf{y}\right]\frac{V(\mathbf{z})\omega^2e^{-i2k|\mathbf{z}-\mathbf{x}_0|}}{(4\pi|\mathbf{z}-\mathbf{x}_0|)^2}F(k,\mathbf{z}\widehat{-}\mathbf{x}_0)\mathrm{d}\mathbf{z}. \tag{16}$$

Putting the unit weight function $W(\omega, \mathbf{y}) = 1$ yields

$$D_{\text{rec}}(\omega) \approx -\int_{\mathbf{z}\in\text{target}} V(\mathbf{z})\omega^2 P(\omega) \frac{e^{-i2k|\mathbf{z}-\mathbf{x}_0|}}{(4\pi|\mathbf{z}-\mathbf{x}_0|)^2} G_a^2(k_0, \widehat{\mathbf{z}-\mathbf{x}_0}, \hat{e})\mathrm{d}\mathbf{z}. \tag{17}$$

The corresponding signal in time domain is

$$d_{\text{rec}}(t) = \frac{1}{2\pi}\int_{-\pi}^{+\pi} D_{\text{rec}}(\omega)e^{i\omega t}\mathrm{d}\omega \approx \int_{\mathbf{z}\in\text{target}} V(\mathbf{z}) \frac{\ddot{p}(t-2|\mathbf{z}-\mathbf{x}_0|/c)}{(4\pi|\mathbf{z}-\mathbf{x}_0|)^2} G_a^2(k_0, \widehat{\mathbf{z}-\mathbf{x}_0}, \hat{e})\mathrm{d}\mathbf{z}, \tag{18}$$

where $\ddot{p}(t)$ is the second derivative of $p(t)$.

2.2.3 *Signal model after removing carrier wave and matched filtering*

Because the received signal $d_{\text{rec}}(t)$ is a radio-frequency signal, we need to remove the carrier frequency ω_0. So, the baseband part is

$$d(t) = d_{\text{rec}}(t)e^{-i\omega_0 t}. \tag{19}$$

It is noted that most of existing SARs make use of linear frequency modulated (LFM) waveform, referred to the chirp signal. That is

$$p(t) = e^{i(\omega_0 t+\pi\gamma t^2)} = e^{i\varphi_0(t)+i\varphi_b(t)}, \qquad |t| < \frac{t_p}{2}, \tag{20}$$

where γ is the frequency ratio and equals to the bandwidth of chirp signal B_a divided by the pulse width in time domain t_p. $\varphi_0(t) = \omega_0 t$, $\varphi_b(t) = \pi\gamma t^2$.

$$\ddot{p}(t) = [-(\omega_0 + 2\pi\gamma t)^2 + i2\pi\gamma]e^{i\varphi_0(t)+i\varphi_b(t)} \qquad |t| < \frac{t_p}{2} \tag{21}$$

Substituting Eqs. (18) and (21) into Eq. (19), we obtain the echoes without carrier frequency

$$\begin{aligned} d(t) &\approx -\int_{\mathbf{z}\in\text{target}} V(\mathbf{z}) \frac{\{[\omega_0 + 2\pi\gamma(t-t_n)]^2 - i2\pi\gamma\}e^{-i\omega_0 t_n + i\varphi_b(t-t_n)}}{(4\pi|\mathbf{z}-\mathbf{x}_0|)^2} G_a^2(k_0, \widehat{\mathbf{z}-\mathbf{x}_0}, \hat{e})\mathrm{d}\mathbf{z}, \\ &\approx -\int_{\mathbf{z}\in\text{target}} V(\mathbf{z}) \frac{\omega_0^2 e^{-i\omega_0 t_n + i\varphi_b(t-t_n)}}{(4\pi|\mathbf{z}-\mathbf{x}_0|)^2} G_a^2(k_0, \widehat{\mathbf{z}-\mathbf{x}_0}, \hat{e})\mathrm{d}\mathbf{z}, \end{aligned} \tag{22}$$

where $t_n = 2|\mathbf{z}-\mathbf{x}_0|/c$.

Until now we just get a one-dimensional range signal when the SAR antenna locates at the position $\mathbf{x}_0$. When the platform moves along some trajectory, $\mathbf{x}_0$, t_n, and $\hat{e}$ may vary with the slow time s, so we just replace $\mathbf{x}_0$, t_n, and $\hat{e}$ by $\mathbf{x}_0(s)$, $t_n(s)$, and $\widehat{e(s)}$ in Eq. (22), and are able to get two-dimensional echoes and matched filtering results:

$$\begin{aligned} d(t,s) &\approx -\int_{\mathbf{z}\in\text{target}} V(\mathbf{z}) \frac{\omega_0^2 e^{-i\omega_0 t_n(s) + i\varphi_b[t-t_n(s)]}}{(4\pi|\mathbf{z}-\mathbf{x}_0(s)|)^2} G_a^2[k_0, \widehat{\mathbf{z}-\mathbf{x}_0(s)}, \widehat{e(s)}]\mathrm{d}\mathbf{z} \\ &= \int_{\mathbf{z}\in\text{target}} V(\mathbf{z}) A[z, \mathbf{x}_0(s), \widehat{\mathbf{e}(s)}] e^{i\varphi_b[t-t_n(s)]}\mathrm{d}\mathbf{z}, \end{aligned} \tag{23}$$

where $A[\mathbf{z}, \mathbf{x}_0(s), \widehat{\mathbf{e}(s)}] = \frac{-\omega_0^2 e^{-i2k_0|\mathbf{z}-\mathbf{x}_0(s)|} G_a^2(k_0, \widehat{\mathbf{z}-\mathbf{x}_0(s)}, \widehat{e(s)})}{(4\pi|\mathbf{z}-\mathbf{x}_0(s)|)^2}$ includes the antenna radiation and some constant terms. Using the stationary phase method,[25] we may get the expression in frequency domain

$$D(\omega,s)\approx\int_{\mathbf{z}\in\text{target}}V(\mathbf{z})A[\mathbf{z},\mathbf{x}_0(s),\widehat{\mathbf{e}(s)}]\mathbf{rect}\left[\frac{\omega-2\pi\gamma t_n}{2\pi\gamma t_p}\right]\frac{e^{-i\left(\frac{\omega^2}{4\pi\gamma}-\frac{\pi}{4}\right)}}{\sqrt{\gamma}}e^{-i2k|\mathbf{z}-\mathbf{x}_0(s)|}\mathrm{d}\mathbf{z}$$
$$=\int_{\mathbf{z}\in\text{target}}e^{-i2k|\mathbf{z}-\mathbf{x}_0(s)|}B(\omega,\mathbf{z},\mathbf{x}_0(s),\widehat{\mathbf{e}(s)})V(\mathbf{z})\mathrm{d}\mathbf{z}, \tag{24}$$

where $B[\omega,\mathbf{z},\mathbf{x}_0(s),\widehat{\mathbf{e}(s)}]=A[\mathbf{z},\mathbf{x}_0(s),\widehat{\mathbf{e}(s)}]\mathbf{rect}\left[\frac{\omega-2\pi\gamma t_n}{2\pi\gamma t_p}\right]\frac{e^{-i\left(\frac{\omega^2}{4\pi\gamma}-\frac{\pi}{4}\right)}}{\sqrt{\gamma}}$. The goal of SAR imaging is to determine $V(\mathbf{z})$ from the echoes $d(t,s)$ or $D(\omega,s)$. The image processor can be thought as an operator of the form

$$I(\mathbf{z}_{xy})=\iint e^{-i2k|\mathbf{z}-\mathbf{x}_0(s)|}Q[k,\mathbf{z},\mathbf{x}_0(s),\widehat{\mathbf{e}(s)}]D(\omega,s)\mathrm{d}\omega\mathrm{d}s, \tag{25}$$

where $\mathbf{z}_{xy}$ is the first two components of $\mathbf{z}=[\mathbf{z}_{xy},0]$ (for the common SARs, one only gets two-dimensional images), $Q[k,\mathbf{z},\mathbf{x}_0(s),\widehat{\mathbf{e}(s)}]$ is an imaging filter chosen by the following formula

$$Q[k,\mathbf{z},\mathbf{x}_0(s),\widehat{\mathbf{e}(s)}]=\frac{\chi(\omega,s,\mathbf{z})B^*(\omega,\mathbf{z},\mathbf{x}_0(s),\widehat{\mathbf{e}(s)})\left|\frac{\partial\boldsymbol{\xi}}{\partial(s,\omega)}\right|}{|B(\omega,\mathbf{z},\mathbf{x}_0(s),\widehat{\mathbf{e}(s)})|^2} \tag{26}$$

where $\chi(\omega,s,\mathbf{z})$ is a window function that prevents division by zero, $\boldsymbol{\xi}=\int_0^1\nabla(2k|R_{\mathbf{x}_0\mathbf{z}}|)|_{\mathbf{x}_0+\mu\mathbf{z}}\approx 2k\mathcal{P}[\widehat{\mathbf{x}_0(s)}-\mathbf{z}]$, with projections operator $\mathcal{P}$ mapping a vector onto its first two components, and $|\frac{\partial\boldsymbol{\xi}}{\partial(s,\omega)}|$ is the Jaccobi determinant.

2.2.4 *Approximation discussions in engineering*

In the above equations, there are a few approximations: the Born approximation in Eq. (6), antenna pattern approximation in Eq. (11), far-field approximation in Eqs. (12), (13), and (16), and amplitude approximation for narrow band signal in Eqs. (21) and (22). Almost all works on radar imaging are involved in making the Born approximation. It makes the nonlinear problem linear.[5,6] The following discussions will focus on the quantitative analysis of the other three approximation errors.

Table 1 Simulation parameters.

Variable	Value
Carrier frequency ω_0	10 GHz
Antenna size $[-a,a]\times[-b,b]$	$[-0.5,0.5]\times[-0.05,0.05]$ m
Pulse width t_P	20 μs
Bandwidth of chirp signal B_w	100 MHz
Platform height H_0	5 km
Incident angle θ_L	45 deg
Pulse repetition frequency f_p	200 Hz
Platform velocity v	100 m $\cdot$ s^{-1}
Radius of flight R_a	2.5 km
Start azimuth angle θ_0	45 deg

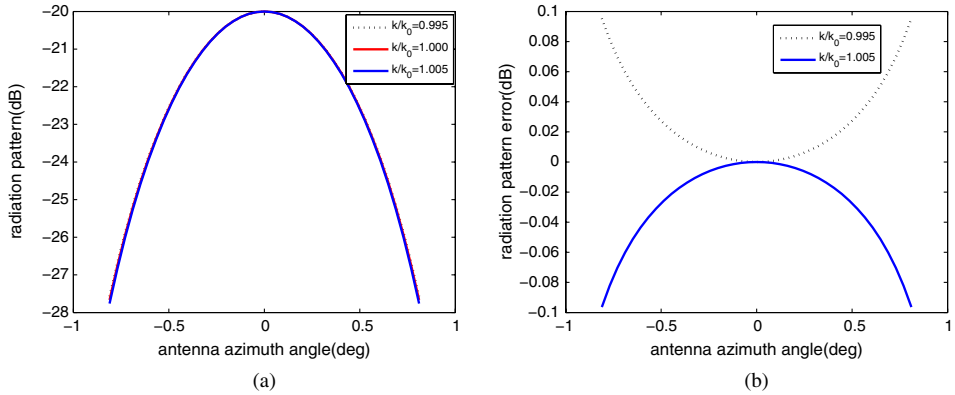

Fig. 1 Antenna pattern with different frequencies within the main lobe: (a) $G(k, \hat{\mathbf{x}}, \hat{e})$ in dB; and (b) $G(k, \hat{\mathbf{x}}, \hat{e}) - G(k_0, \hat{\mathbf{x}}, \hat{e})$ in dB.

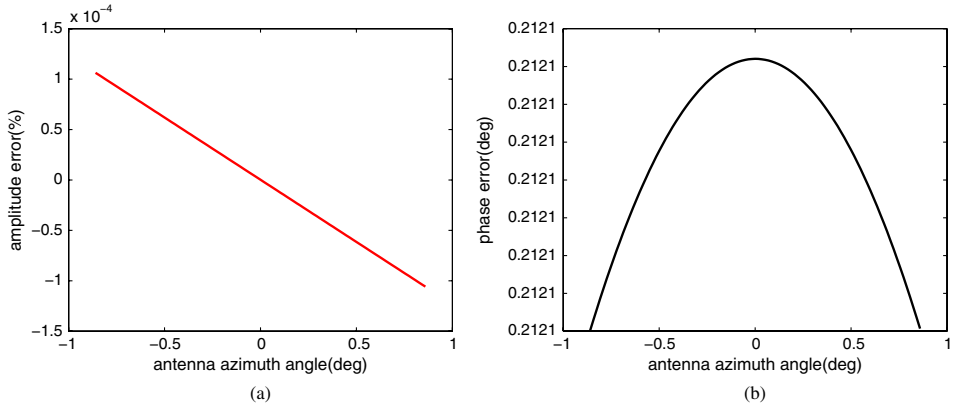

Fig. 2 Far-filed approximation errors: (a) amplitude error in percentage; and (b) phase error in degree.

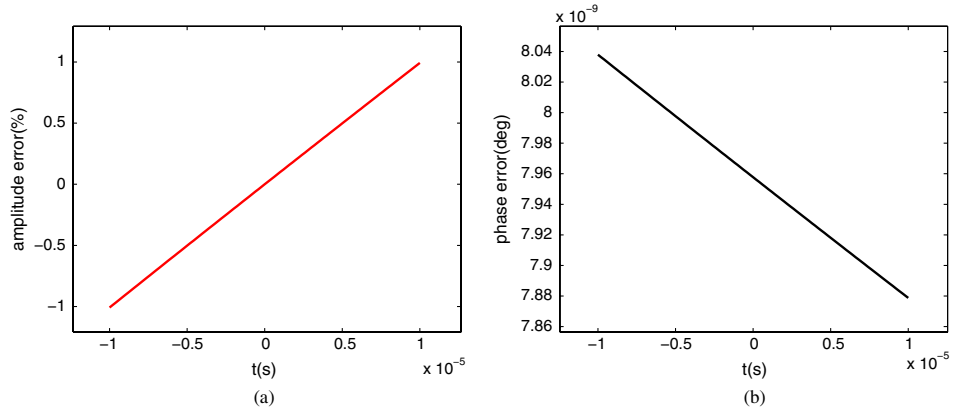

Fig. 3 Narrow bandwidth approximation errors: (a) amplitude error in percentage; and (b) phase error in degree.

Under the parameters in Table 1, the varying range of $\frac{k}{k_0}$ is (0.995, 1.005), and Fig. 1 displays the effect by the antenna pattern approximation. We can see the approximation error is very small, which is less than 0.1 dB within the main lobe. So we may replace $G(k, \hat{\mathbf{x}}, \hat{e})$ by $G(k_0, \hat{\mathbf{x}}, \hat{e})$ for engineering applications.

Usually the distance between the target and the antenna is many times the wavelength or the antenna's length. So, $|\mathbf{z} - \mathbf{x}_0| \gg |\mathbf{y} - \mathbf{x}_0|$, where $\mathbf{x}_0$ is the position of antenna phase center, $\mathbf{y}$ is

the position of some point in the antenna, and $\mathbf{z}$ is the target position on the ground. Then we may use the far-field approximation $|\mathbf{y}-\mathbf{z}| \approx |\mathbf{z}-\mathbf{x}_0| - (\widehat{\mathbf{z}-\mathbf{x}_0}) \cdot (\mathbf{y}-\mathbf{x}_0)$. In Eq. (12) and those equations thereafter, the amplitude $\frac{1}{|\mathbf{y}-\mathbf{z}|}$ is replaced by $\frac{1}{|\mathbf{z}-\mathbf{x}_0|-(\widehat{\mathbf{z}-\mathbf{x}_0})\cdot(\mathbf{y}-\mathbf{x}_0)} \approx \frac{1}{|\mathbf{z}-\mathbf{x}_0|}$, and the phase term $e^{ik|\mathbf{y}-\mathbf{z}|}$ is replaced by $e^{ik|\mathbf{z}-\mathbf{x}_0|-(\widehat{\mathbf{z}-\mathbf{x}_0})\cdot(\mathbf{y}-\mathbf{x}_0)|}$. Figure 2 shows the errors by the far-field approximation. We see that the amplitude errors are so small that they may be neglected. The phase error is less than 1 deg and also very small.

Thirdly, we will illustrate the narrow bandwidth approximation. In fact, the errors just occur when one replaces $\ddot{p}(t)$ by $-\omega_0^2 p(t)$. Fortunately, it just generates small amplitude and phase errors. Figure 3 shows the errors by this approximation. We can see that the amplitude error is less than 1%. The phase error is less than 10^{-8} degree.

So far, we understand that the common signal expressions in engineering are the special cases with depressing some complex constants. The following expression is usually used for discrete point targets,

$$d(t,s) = \sum \sigma_n p_0\left[t - \frac{2R_n(s)}{c_0}\right] \exp\left\{-\frac{i4\pi R_n(s)}{\lambda}\right\}, \tag{27}$$

where σ_n is the radar cross section of the nth target, $p_0(t) = \exp\{i\varphi_b(t)\} = \exp\{i\pi\gamma t^2\}$ is the base band chirp signal, and R_n is the slant range between the nth target and the antenna phase center at the slow time s, $\lambda = \frac{2\pi c_0}{\omega_0}$ is the wavelength.

After these approximations, the engineers could concentrate on the imaging algorithms much more easily.

3 Outer-CSAR Signal Model and Imaging Algorithm

3.1 *Outer-CSAR System Model*

When an outer-CSAR works, the platform of SAR moves along a circle and the beam of the antenna points to the outer circle. That means the SAR works on the original left (or right) side-looking to the right (or left) side-looking. While the platform fully moves along a circle, a cirque scene can be illustrated, and we can observe many more targets at the same time. Figure 4 displays the imaging system geometry for an outer-CSAR. The position of antenna $\mathbf{x}_0(s)$ is $(R_a \cos\theta_a, R_a \sin\theta_a, H_0)$, and the target P is located at $\mathbf{z} = (r_p \cos\theta_p, r_p \sin\theta_p, 0)$. Suppose that the platform moves at the same angular velocity ω_a, then $\theta_a = \theta_0 + \omega_a s$, where θ_0 is the initial azimuth angle and s is the slow time.

Because the radar moves along a circular trajectory, the antenna directions change all the times. That means the antenna direction vector $\hat{e}$ changes pulse by pulse. For simplicity, we just consider $G_a(k_0, \hat{\mathbf{x}}, \hat{e}) = 4ab$ within the main lobe in the azimuth and range directions. Then

$$G_a[k_0, \mathbf{z} - \widehat{\mathbf{x}_0(s)}, \widehat{e(s)}] = 4ab\,\mathbf{rect}\left(\frac{\theta_0 + \omega_a s - \theta_p}{\theta_A}\right), \tag{28}$$

where $\theta_A \approx \frac{\pi c_0}{\omega a}$ is the azimuth beamwidth.

3.2 *Imaging Method*

According to the above equations, we have

$$\xi = 2k\mathcal{P}[\widehat{\mathbf{x}_0(s)} - \mathbf{z}] = 2k\frac{[R_a \cos\theta_a - r_p \cos\theta_p, R_a \sin\theta_a - r_p \sin\theta_p]}{R_{\mathbf{xz}}}, \tag{29}$$

$$\left|\frac{\partial \boldsymbol{\xi}}{\partial(s,\omega)}\right| = \frac{4\omega\omega_a R_a[r_p \cos(\theta_a - \theta_p) - R_a]}{c_0^2 R_{\mathbf{xz}}}, \tag{30}$$

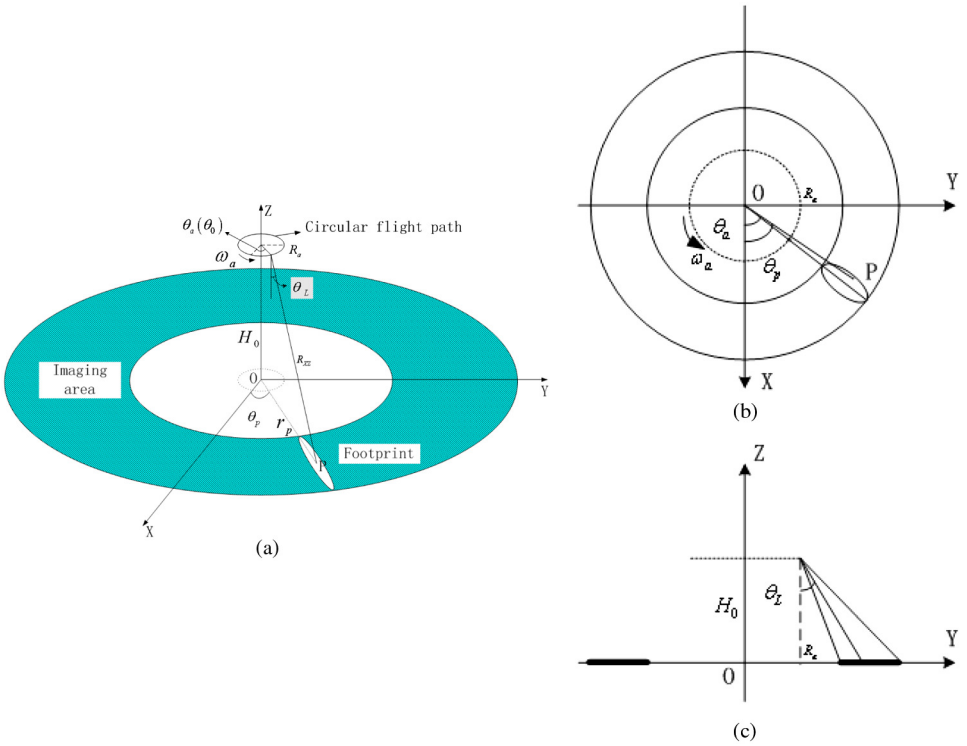

Fig. 4 Imaging system geometry in outer-CSAR: (a) three-dimensional chart; and (b) top-view chart; (c) side-view chart.

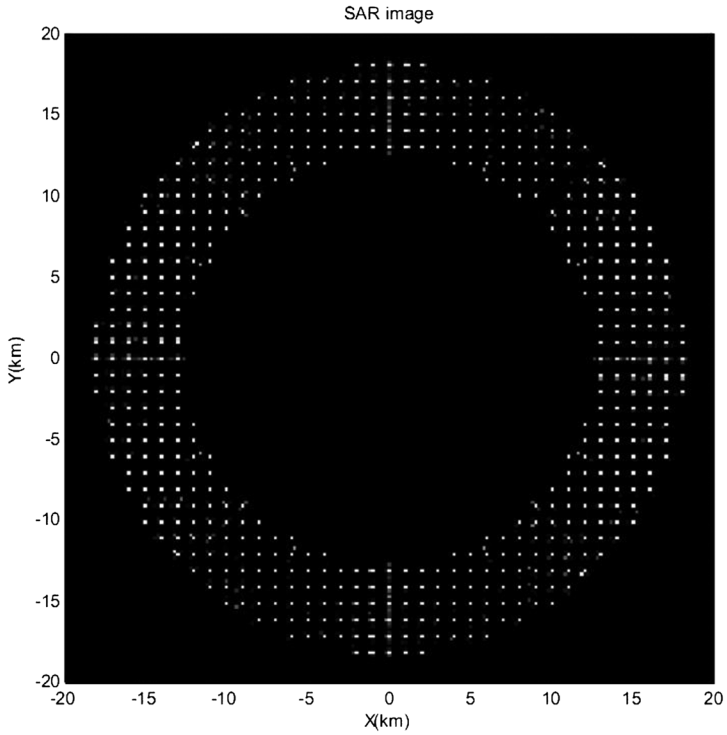

Fig. 5 Imaging results of a outer-CSAR.

where $R_{\mathbf{xz}} = \sqrt{R_a^2 + r_p^2 - 2R_a r_p \cos(\theta_a - \theta_p) + H_0^2}$.

Then, the filter is

$$Q[k, \mathbf{z}, \mathbf{x}_0(s), \widehat{\mathbf{e}(s)}] = \mathbf{rect}\left(\frac{\omega - 2\pi\gamma t_n}{2\pi\gamma t_p}\right)\mathbf{rect}\left(\frac{\theta_0 + \omega_a s - \theta_p}{\theta_A}\right) \cdot \frac{4\pi^2\sqrt{\gamma}\omega\omega_a R_a[R_a - r_p \cos(\theta_0 + \omega_a s - \theta_p)]R_{\mathbf{xz}} e^{i\left(2kR_{\mathbf{xz}} + \frac{\omega^2}{4\pi\gamma} - \frac{\pi}{4}\right)}}{(ab\omega_0 c_0)^2}. \tag{31}$$

Substituting Eq. (31) into Eq. (25), we are able to get the image for an outer-CSAR.

4 Simulation

Table 1 lists the main simulation parameters in this paper. According to the given parameters, $\gamma = \frac{B_w}{t_p} = 5 \times 10^{12}$ s^{-2}, $\omega_a = \frac{v}{R_a} = 0.04$ rad/s.

We set a point array as a target on the ground, and the distance between X and Y is 500 m. After transmitting chirp signals and receiving echoes, we adopt the filtered back projection algorithm with the filter Eq. (31) to get the imaging result displayed in Fig. 5.

From the imaging results, we can see that the outer-CSAR can inform a cirque SAR image and the image area is much bigger than the general CSAR pointing at the center of the projection from the path. The point targets are focused in both azimuth and range directions.

5 Conclusion

In this paper, we derived the SAR signal model from the scalar form of Maxwell's equations. We can use some approximations in engineering applications when the approximation errors are neglected. The new operation Outer-CSAR and its imaging algorithm are presented. The imaging result displayed that the Outer-CSAR is useful for wide observation.

Acknowledgments

The author (B. Sun) expresses his great appreciation to professor Qiao's team for their discussions on the PDEs and SAR imaging. The author also thanks the software systems specialist Robert C. Jackson of UTPA for the parallel computation. This research is supported by the Fundamental Research Funds for the Central Universities. This work (Z. Qiao) is also supported by the U. S. Army Research Office under contract/grant No. W911NF-08-1-0511 and by the Texas Norman Hackerman Advanced Research Program under Grant No. 003599-0001-2009.

References

1. G. Franceschetti and R. Lanari, *Synthetic Aperture Radar Processing*, CRC Press LLC, Boca Raton (1999).
2. F. D. Zan and A. M. Guarnieri, "TOPSAR: terrain observation by progressive scans," *IEEE Trans. Geosci. Remote Sens.* **44**(9), 2352–2360 (2006), http://dx.doi.org/10.1109/TGRS.2006.873853.
3. M. Soumekh, *Synthetic Aperture Radar Signal Processing with MATLAB Algorithms*, Wiley, New York (1999).
4. H. R. Srivastava, P. Patel, and R. R. Navalgund, "How far SAR has fulfilled its expectation for soil moisture retrieval," *Proc. SPIE* **6410**, 641001 (2006) http://dx.doi.org/10.1117/12.693946.
5. H.S. Srivastava et al., "Explored and demonstrated potential applications of multi-parametric SAR in context of Keoladeo National Park, BHARATPUR, INDIA," in *Proc. 2nd ARS-KNP*, Bharatpur, India, pp. 01–30 (2009), www.ramsar.org/pdf/features/features/remote/keoladeo.pdf.

6. M. C. Dobson et al., "Estimation of forest biophysical characteristics in Northern Michigan with SIR-C/X-SAR," *IEEE Trans. Geosci. Remote Sens.* **33**(04), 877–895 (1995), http://dx.doi.org/10.1109/36.406674.
7. S.H. Shanker et al., "Multi-frequency and multi-polarized SAR response to thin vegetation and scattered trees," *Curr. Sci.* **97**(3), 425–429 (2009).
8. P. Patel, H.S. Srivastava, and R.R. Navalgund, "Estimating wheat yield: an approach for estimating number of grains using cross-polarised ENVISAT-1 ASAR data," *Proc. SPIE* **6410**, 641009 (2006), http://dx.doi.org/10.1117/12.693930.
9. M. C. Dobson et al., "Dependence of radar backscatter on coniferous forest biomass," *IEEE Trans. Geosci. Remote Sens.* **30**(2), 412–415 (1992), http://dx.doi.org/10.1109/36.134090.
10. G. Picard, T. Le Toan, and F. Mattia, "Understanding C-band radar backscatter from wheat canopy using a multiple-scattering coherent model," *IEEE Trans. Geosci. Remote Sens.* **41**(7), 1583–1591 (2003), http://dx.doi.org/10.1109/TGRS.2003.813353.
11. P. Parul, S.H. Shanker, and N.R. Ranganath, "Use of synthetic aperture radar polarimetry to characterize wetland targets of Keoladeo National Park, Bharatpur, India," *Curr. Sci.* **97**(4), 529–537 (2009).
12. P. Patel et al., "Comparative evaluation of the sensitivity of multi-polarized multi-frequency SAR backscatter to plant density," *Int. J. Rem. Sens.* **27**(2), 293–305 (2006), http://dx.doi.org/10.1080/01431160500214050.
13. M. C. Dobson, F. T. Ulaby, and L. E. Pierce, "Land-coverclassification and estimation of terrain attributes using synthetic aperture radar," *Rem. Sens. Environ.* **51**(1), 199–214 (1995), http://dx.doi.org/10.1016/0034-4257(94)00075-X.
14. S.H. Shanker, P. Parul, and N.R. Ranganath, "Application potentials of synthetic aperture radar interferometry for land-cover mapping and crop-height estimation," *Curr. Sci.* **91**(6), 783–788 (2006).
15. H. S. Srivastava et al., "Comparative evaluation of potential of optical and SAR data for the detection of human settlements using digital classification," *Int. J. Geoinform.* **2**(3), 21–28 (2006).
16. Z.-G. Xia and F. M. Henderson, "Understanding the relationships between radar response patterns and the bio- and geophysical parameters of urban areas," *IEEE Trans. Geosci. Remote Sens.* **35**(1), 93–101 (1997), http://dx.doi.org/10.1109/36.551938.
17. W. L. Stutzman, *Antenna Theory and Design*, John Wiley & Sons, Canada (1981).
18. M. Cheney, "A mathematical tutorial on synthetic aperture radar," *SIAM Rev.* **43**(2), 301–312 (2001), http://dx.doi.org/10.1137/S0036144500368859.
19. M. Cheney and B. Borden, *Fundamentals of Radar Imaging*, SIAM, Philandelphia (2009).
20. C. J. Nolan and M. Cheney, "Synthetic aperture inversion," *Inverse Problems* **18**(1), 221–235 (2002), http://dx.doi.org/10.1088/0266-5611/18/1/315.
21. G. Garza, J. X. Lopez, and Z. Qiao, "Cross-range imaging of synthetic aperture radar data," *Pacific J. Appl. Math. PJAM 2009* **2**(3), 65–81 (2009).
22. J. X. Lopez and Z. Qiao, "Filtered back projection inversion of turntable ISAR data," *Proc. SPIE* **8051**, 805109 (2011), http://dx.doi.org/10.1117/12.884419.
23. L. Debnath, *Linear Partial Differential Equations for Scientists and Engineers*, Birkhauser, Boston (2007).
24. K. J. Langenberg et al., "Principles of microwave imaging and inverse scattering," *EARSeL Adv. Rem. Sens.* **2**(1–I), 163–186 (1993).
25. A. Papoulis, *Signal Analysis*, McGraw-Hill Book Inc., New York (1977).

Bing Sun received his BS and PhD degrees from Beihang University, Beijing, China, in 2003 and 2008, respectively. Since 2010, he has been a lecturer with the School of Electronic and Information Engineering, Beihang University. His current research interests include modeling, simulation, and imaging algorithms for multiplatform SAR systems. In 2011, he was a visiting researcher in the Department of Mathematic, the University of Texas-Pan American (UTPA).

Zhijun Qiao received his PhD degree in applied math from the Institute of Mathematics, Fudan University, Shanghai, China, in 1997. From 1999 to 2001, he was a Humboldt Research Fellow with the Department of Mathematics and Computer Science, University of Kassel. From 2001 to 2004, he was a researcher with the Theoretical Division, Los Alamos National Laboratory. Since 1997 and is currently with the Department of Mathematics, UTPA. His research interests include nonlinear PDEs and radar imaging.

Jie Chen received his BS and PhD degrees from Beihang University, Beijing, China, in 1996 and 2002, respectively. Since 2011, he has been a professor with the School of Electronic and Information Engineering, Beihang University. His current research interests include remote sensing information acquisition and signal processing; topside ionosphere exploration based on spaceborne HF-SAR; high-resolution spaceborne SAR image formation; and modeling and simulation for spaceborne SAR systems.